

A note on thermomechanical coupling effects in the indentation of pseudoelastic shape memory alloys

Mohsen Rezaee-Hajidehi^{a,*}, Mahdi Neghabi^a, Stanisław Stupkiewicz^a

^a*Institute of Fundamental Technological Research (IPPT), Polish Academy of Sciences, Pawińskiego 5B, 02-106 Warsaw, Poland.*

Abstract

While macroscopic experiments on polycrystalline shape memory alloys (SMAs) reveal significant thermomechanical coupling effects arising from the latent heat of transformation, the relevance of thermomechanical couplings in indentation tests remains ambiguous. This ambiguity is further emphasized by the rate effects observed in a number of micro/nano-indentation experiments, thus highlighting the need for a more careful investigation of the thermomechanical interactions at such small scales. With this in mind, the present study aims to demonstrate the role of thermomechanical couplings in indentation-induced martensitic transformation in SMAs. To this end, a simple phenomenological model of pseudoelasticity is employed and finite-element simulations are performed to address two key questions. (1) At which spatial and temporal scales do the thermomechanical couplings arising from the latent heat become effective? (2) To what extent do these couplings influence the indentation response? In connection with the latter, our analysis quantifies the maximal thermal effects that emerge during adiabatic indentation and compares them with those of isothermal indentation.

Keywords: Pseudoelasticity; Indentation; NiTi; Latent heat; Thermomechanical interactions

1. Introduction

At macroscopic scale, shape memory alloys (SMAs) exhibit a rate-dependent behavior. The rate-dependence is primarily driven by thermomechanical interactions originating from the latent heat of martensitic phase transformation. This is manifested under non-isothermal loading conditions, where the generated latent heat is not completely removed from the specimen due to the limited heat exchange with the surroundings. Accordingly, the resulting temperature rise elevates the transformation stress (in accordance with the Clausius–Clapeyron relation) and thus leads to complex transformation evolutions [1–4].

*Corresponding author.

Email addresses: mrezaee@ippt.pan.pl (Mohsen Rezaee-Hajidehi), mneghabi@ippt.pan.pl (Mahdi Neghabi), sstupkie@ippt.pan.pl (Stanisław Stupkiewicz)

Micro/nano-indentation tests have been extensively used to probe the microstructural features and small-scale mechanical properties of SMAs, e.g., [5–8]. Within this context, a number of experiments have explored the effect of indentation loading rate on the deformation behavior of the material [8–11]. Notably, in some cases, a rate-dependent behavior has been observed, which has been occasionally attributed to the thermomechanical interactions. It is, however, important to acknowledge that at such small scales, heat conduction is dominant, and the generated latent heat is expected to be rapidly transferred away from the indented region, hence leading to a (nearly) uniform temperature distribution. As a consequence, it can be reasonably inferred that thermomechanical interactions are less likely to be the origin of rate effects in micro/nano-indentation. Nevertheless, the ambiguity surrounding the potential contribution of thermomechanical couplings at small scales underscores the need for further investigation.

The present study aims to elucidate the role of thermomechanical couplings in the indentation-induced martensitic transformation in SMAs. Our investigation is based on a simple phenomenological model of pseudoelasticity and is performed in two steps. First, we employ a thermomechanically-coupled model to assess the significance of transient thermomechanical interactions across various spatial and temporal scales. The goal of this initial analysis is to address the question of when and how do the thermal effects arising from the latent heat of transformation come into play during the indentation of SMAs. Subsequently, we further simplify the model and explore the potential thermal effects during adiabatic indentation. The goal of this analysis is to provide an upper-bound of these thermal effects. The study concludes with a summary of the simulation results and some general remarks.

2. Thermal Effects during Indentation of SMAs

This section begins with a brief description of the thermomechanically-coupled model of pseudoelasticity, followed by the presentation and discussion of the simulation results.

2.1. Thermomechanically-Coupled Model of Pseudoelasticity

A small-strain model of pseudoelasticity is employed. The model can be considered as a simplified non-gradient version of the model developed by Rezaee-Hajidehi et al. [12]. Formulated within the incremental energy minimization framework, the constitutive description relies on two main elements: the Helmholtz free energy function ϕ and the dissipation potential D . For simplicity, it is assumed that ϕ comprises only two components, namely the chemical energy ϕ_{chem} and the elastic strain energy ϕ_{el} . This assumption leads to a flat (neither hardening- nor softening-type) flag-shaped material response within the transformation regime. At the same time, the dissipation potential D accounts solely for the dissipation due to martensitic phase transformation, while

neglecting dissipation due to martensite reorientation. Following [12, 13], the model incorporates thermomechanical coupling through the chemical energy ϕ_{chem} and through the internal heat source associated with phase transformation in the heat conduction equation. The model formulation is presented below.

In the small-strain setting, the total strain $\boldsymbol{\varepsilon}$ is additively decomposed into the elastic and transformation parts,

$$\boldsymbol{\varepsilon} = \boldsymbol{\varepsilon}^e + \boldsymbol{\varepsilon}^t. \quad (1)$$

The transformation strain $\boldsymbol{\varepsilon}^t$ is defined in terms of two internal variables, the transformation strain of fully-oriented martensite, $\bar{\boldsymbol{\varepsilon}}^t$, and the volume fraction of martensite, η , i.e.,

$$\boldsymbol{\varepsilon}^t = \eta \bar{\boldsymbol{\varepsilon}}^t, \quad \bar{\boldsymbol{\varepsilon}}^t \in \bar{\mathcal{P}} = \{ \bar{\boldsymbol{\varepsilon}}^t : g(\bar{\boldsymbol{\varepsilon}}^t) = 0 \}, \quad 0 \leq \eta \leq 1, \quad (2)$$

where the set $\bar{\mathcal{P}}$ of admissible limit transformation strains is represented by the surface $g(\bar{\boldsymbol{\varepsilon}}^t) = 0$, and the volume fractions $\eta = 0$ and $\eta = 1$ indicate the pure austenite and pure martensite phases, respectively. It is here assumed that the martensitic transformation is isochoric, implying $\text{tr} \bar{\boldsymbol{\varepsilon}}^t = 0$, where tr denotes the trace of a tensor. Additionally, we postulate that the transformation is isotropic and exhibits no tension–compression asymmetry. Consequently, the function $g(\bar{\boldsymbol{\varepsilon}}^t)$ depends solely on the second invariant I_2 of the limit transformation strain $\bar{\boldsymbol{\varepsilon}}^t$, cf. [14], and is defined as

$$g(\bar{\boldsymbol{\varepsilon}}^t) = \sqrt{-I_2} - a, \quad I_2 = -\frac{1}{2} \text{tr}(\bar{\boldsymbol{\varepsilon}}^t)^2, \quad (3)$$

where $a = \sqrt{3}/2\epsilon_T$, with ϵ_T representing the maximum attainable transformation strain. It is worth mentioning that the omitted features, namely tension–compression asymmetry and transverse isotropy, are accounted for in the original (finite-strain) model. For further details, see [12].

As mentioned above, only the contributions from the chemical energy and the elastic strain energy are considered in the Helmholtz free energy function ϕ , i.e.,

$$\phi(\boldsymbol{\varepsilon}, \bar{\boldsymbol{\varepsilon}}^t, \eta, T) = \phi_{\text{chem}}(\eta, T) + \phi_{\text{el}}(\boldsymbol{\varepsilon}, \bar{\boldsymbol{\varepsilon}}^t, \eta). \quad (4)$$

The chemical energy ϕ_{chem} is given by

$$\phi_{\text{chem}}(\eta, T) = \phi_0^a(T) + \Delta\phi_0(T)\eta, \quad \Delta\phi_0(T) = \Delta s^*(T - T_t), \quad (5)$$

where T is the temperature, ϕ_0^a is the free energy density of unstressed pure austenite phase, Δs^* is the specific entropy difference, and T_t is the transformation equilibrium temperature. The linear dependence of the chemical energy ϕ_{chem} on the temperature T through $\Delta\phi_0$ expresses the Clausius–Clapeyron relation and results in a linear dependence between the temperature and the transformation stress [15].

The elastic strain energy ϕ_{el} takes the form

$$\phi_{\text{el}}(\boldsymbol{\varepsilon}, \bar{\boldsymbol{\varepsilon}}^t, \eta) = \mu \text{tr}(\boldsymbol{\varepsilon}_{\text{dev}}^e)^2 + \frac{1}{2} \kappa (\text{tr} \boldsymbol{\varepsilon}^e)^2, \quad (6)$$

where $\boldsymbol{\varepsilon}^e = \boldsymbol{\varepsilon} - \boldsymbol{\varepsilon}^t$ and $\boldsymbol{\varepsilon}_{\text{dev}}^e$ is its deviatoric part, μ is the shear modulus and κ is the bulk modulus. Although the shear modulus μ typically varies with the volume fraction η , due to the distinct elastic properties of the austenite and martensite phases, we assume for simplicity that μ remains constant during the transformation.

Next, a rate-independent dissipation potential is adopted in the following (incremental) form,

$$\Delta D(\Delta\eta) = f_c |\Delta\eta|, \quad (7)$$

where $\Delta\eta = \eta - \eta_n$, with η_n as the martensite volume fraction related to the previous time-step, and f_c is the critical driving force for transformation, a parameter that characterizes the width of the hysteresis loop.

With the Helmholtz free energy ϕ and the dissipation potential ΔD at hand, their global counterparts are constructed, i.e., $\Phi = \int_B \phi \, dV$ and $\Delta\mathcal{D} = \int_B \Delta D \, dV$. A global incremental potential Π is then formulated by summing the global incremental energy $\Delta\Phi$, the global dissipation potential $\Delta\mathcal{D}$, and the potential of external loads $\Delta\Omega$ (left unspecified here). Subsequently, at a given temperature T , the solution of the problem in terms of the displacement \boldsymbol{u} , the limit transformation strain $\bar{\boldsymbol{\varepsilon}}^t$ and the martensite volume fraction η is sought through the minimization of the incremental potential Π . This is expressed as

$$\Pi = \Delta\Phi + \Delta\mathcal{D} + \Delta\Omega \rightarrow \min_{\boldsymbol{u}, \bar{\boldsymbol{\varepsilon}}^t, \eta} \quad (\text{at a given } T). \quad (8)$$

Note that the minimization problem (8) is subject to equality and inequality constraints on the internal variables $\bar{\boldsymbol{\varepsilon}}^t$ and η , see Eq. (2)_{2,3}.

To complete the model, the temperature T is determined by solving the heat conduction equation. A full thermomechanically-coupled model is achieved by formulating the internal heat source \dot{R} such that two main heat sources are accounted for, namely the latent heat of transformation and the heat generated by mechanical dissipation. Thus, \dot{R} takes the form

$$\dot{R} = \Delta s^* T \dot{\eta} + f_c |\dot{\eta}|, \quad (9)$$

where $\dot{\eta} = \Delta\eta/\Delta t$ in the incremental setting. The (isotropic) heat conduction equation is then given by

$$\varrho_0 c \dot{T} + \nabla \cdot \boldsymbol{q} = \dot{R}, \quad \boldsymbol{q} = -k \nabla T, \quad (10)$$

where $\varrho_0 c$ is the specific heat capacity, k is the heat conduction coefficient, both assumed identical for austenite and martensite phases, and \boldsymbol{q} is the heat flux. It is important to note that, in this study, the heat exchange between the material and the indenter as well as the heat convection with the ambient are neglected. Incorporating these heat exchange processes would reduce the thermal effects, hence the present analysis offers an upper bound estimation of the thermal interactions.

The minimization problem (8) can be reformulated into a global–local minimization problem, wherein the minimization with respect to the limit transformation strain $\bar{\boldsymbol{\varepsilon}}^t$ and the martensite volume fraction η is carried out locally at each Gauss point. As a result, the model includes two global fields, the displacement \boldsymbol{u} and the temperature T .

The indentation problem under consideration is approached using an axisymmetric finite-element formulation. Linear 4-noded quadrilateral elements are utilized for both the displacement \boldsymbol{u} and the temperature T . The computer implementation of the model is done by means of the automatic differentiation technique in AceGen, and the finite-element simulations are performed in AceFEM [16]. Note that in the present simulations, the indenter is assumed to be rigid and frictionless. The corresponding contact problem is thus solved through enforcing the unilateral contact (impenetrability) condition on the potential contact surface using the augmented Lagrangian method [17].

2.2. Thermomechanical Analysis

The model described above is now applied to the problem of indentation of a polycrystalline NiTi. We analyze the temperature variation and its impact on the indentation-induced martensitic transformation across a broad range of spatial and temporal scales. Our primary objective is to identify the specific scales at which the transient thermal effects become substantial. Note that the spatial and temporal dependencies of the problem at hand can be readily recognized through the thermal diffusivity coefficient, which is defined as $k/(\rho_0 c)$ and has the unit of square length per time (m^2/s).

We perform a series of simulations where the indenter radius R is varied from 0.05 mm to 50 mm, thus covering a wide range of spatial scales from micro/nano-indentation to macro-indentation, and the indentation speed v is varied from 0.1 $\mu\text{m}/\text{s}$ to 100 $\mu\text{m}/\text{s}$, which is wide enough to encompass the range of practical speeds in quasi-static indentation tests, see e.g., [8, 9]. Note that the indenter radius of 50 mm exceeds the practical size of the indenter typically used in the experiment, and it is included here to make the study more complete.

The simulations are performed on a computational domain of the size $L \times L$, see Fig. 1. To preserve the geometrical similarity in all the simulations, the geometrical ratio of $L/R = 6$ is kept fixed. Our preliminary analysis showed that the ratio $L/R = 6$ is sufficiently large to avoid the spurious effects arising from the boundaries. A non-uniform finite-element mesh is employed in which the area beneath the indenter possesses the finest mesh, with a ratio of $h/R = 1.4 \times 10^{-3}$, where h denotes the element size. The mesh gradually coarsens away from the indenter. In all the simulations, the loading is exerted up to a maximum normalized indentation depth of $\delta_{\max}/R = 0.04$. In experiments, larger indentation depths would likely induce plastic deformation, thereby spoiling the pure pseudoelastic behavior.

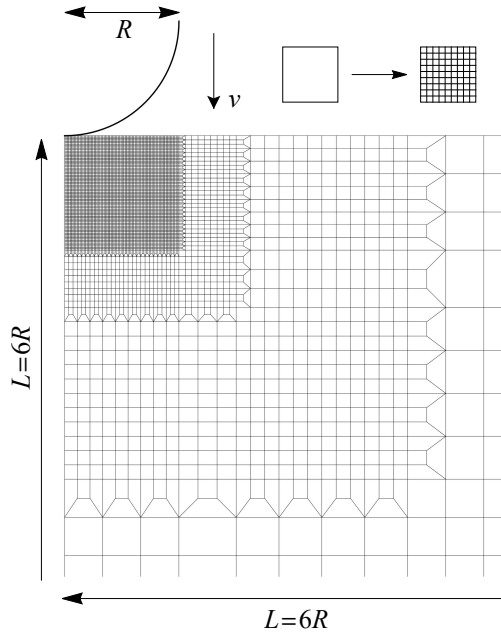


Figure 1: Simulation setup for the axisymmetric indentation problem. The 2D mesh depicted here is 9 times coarser than the mesh actually used in the simulations, see the inset. To enhance the visibility of the mesh in the vicinity of the indenter, the entire computational domain is not displayed.

The material parameters are set as follows: Young’s modulus $E = 41$ GPa, Poisson’s ratio $\nu = 0.3$, maximum transformation strain $\epsilon_T = 0.039$ (within the typical range for NiTi in compression), specific entropy difference $\Delta s^* = 0.24$ MPa/K, equilibrium temperature $T_t = 255$ K, and critical driving force $f_c = 4.6$ MPa. Parameters governing the heat transfer are taken from our previous studies [12, 13], namely specific heat capacity $\rho_0 c = 2.86$ MJ/(m³ K) and heat conduction coefficient $k = 18$ W/(m K). The initial temperature is set to $T_0 = 293$ K.

The simulation results indicate that at small spatial scales, the temperature distribution remains nearly uniform, with the relative temperature change $\theta = T - T_0$ consistently below 1 K. This expected observation aligns with the dominant role of heat conduction at small spatial scales. As the spatial scale increases, θ becomes more pronounced, which then leads to the deviation of the load–indentation depth response from the isothermal case. This effect is illustrated in Fig. 2 for the largest spatial scale with $R = 50$ mm. It follows that at an indentation speed of $v = 100$ $\mu\text{m/s}$, the normalized load at the maximum indentation depth exhibits an increase of about 15 MPa compared to the isothermal scenario, which stems from thermal hardening effects. Notably, during unloading, the indentation response follows a somewhat different trajectory, intersecting with the isothermal response at $\delta/R = 0.02$. Interestingly, despite a maximum relative temperature of about $\theta_{\max} = 14$ K at $v = 100$ $\mu\text{m/s}$, the distribution of martensite volume fraction η seems to be

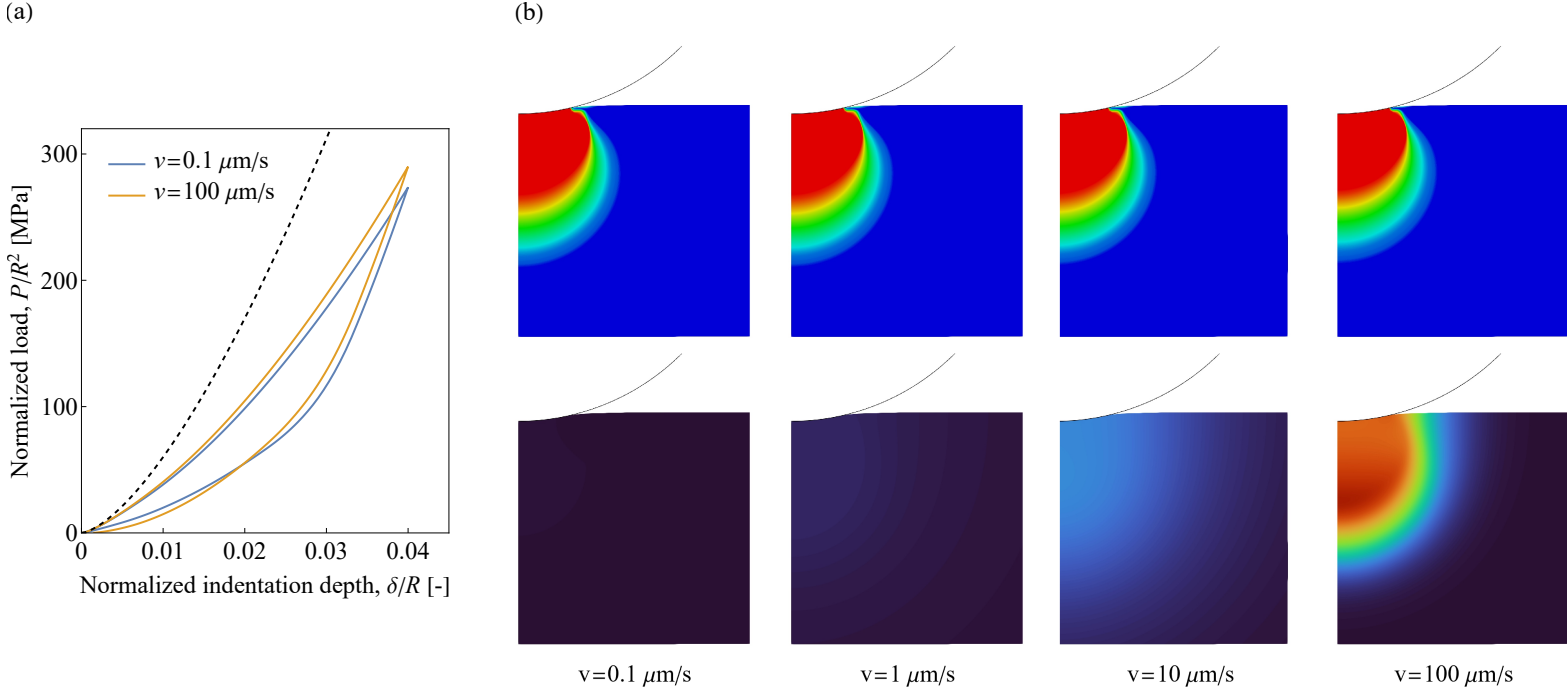


Figure 2: Thermomechanically-coupled analysis of indentation-induced martensitic transformation: the effect of indentation speed v on (a) normalized load–indentation depth response, and (b) spatial distribution of martensite volume fraction η and relative temperature $\theta = T - T_0$. The results pertain to the indentation problem with the largest spatial scale, namely $R = 50$ mm. The dashed curve in panel (a) shows the elastic response. The snapshots in panel (b) are taken at the maximum indentation depth of $\delta_{\text{max}}/R = 0.04$.

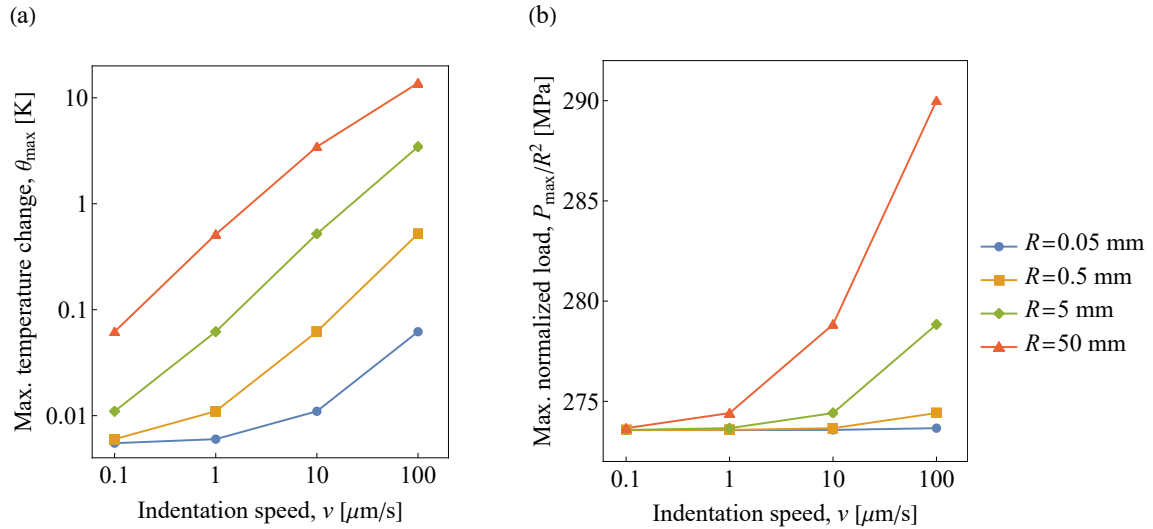


Figure 3: Thermomechanically-coupled analysis of indentation-induced martensitic transformation: the maximum relative temperature θ_{max} (a) and the maximum normalized load P_{max}/R^2 (b) as a function of the indentation speed v for different spatial scales. The data correspond to the maximum indentation depth of $\delta_{\text{max}}/R = 0.04$.

unaffected and closely resembling that of the isothermal case.

As a summary of this analysis, Fig. 3 depicts the variation of the maximum relative temperature θ_{\max} and the maximum normalized load P_{\max}/R^2 with respect to the indentation speed v for different spatial scales. The normalization of the indentation load by R^2 produces a stress-like quantity that filters out first-order geometrical (size) effects, and thus enables us to isolate and examine the impact of thermomechanical coupling on the indentation response across varying spatial scales. It is important to note from Fig. 3 that the maximum relative temperature, reaching about $\theta_{\max} = 14$ K, remains visibly lower than $\theta_{\max} = 27.5$ K obtained under adiabatic condition (see Fig. 4(a) in the subsequent section). This indicates that achieving adiabatic indentation would require much higher loading rates, higher than those feasible in quasi-static indentation experiments.

3. Thermal Effects during Adiabatic Indentation

A key takeaway from the preceding analysis is that within the micro/nano spatial scales and at typical quasi-static indentation speeds, transient thermal effects and the resulting thermomechanical interactions are negligible. Nevertheless, in this section, with the aim to gain more insight into the thermomechanical aspects of the problem, a hypothetical scenario of adiabatic indentation is considered and the goal is to determine the extent to which thermal effects can contribute to the indentation behavior of SMAs. In what follows, we first describe the methodology used in this analysis and then discuss the corresponding results.

3.1. A Simplified Approach for Adiabatic Indentation

Our methodology follows the work of Stupkiewicz [18], see Section 8.3.4 therein. It is based on the assumption that the adiabatic condition manifests exclusively in the increase of the transformation stress during the exothermic forward phase transformation, and analogously, in the decrease of the transformation stress during the endothermic reverse phase transformation. Accordingly, the model presented in Section 2.1 is simplified by treating the temperature T as a dependent variable rather than an independent degree of freedom. The evolution of T is then derived explicitly from the adiabatic heat balance equation, cf. Eq. (10) with $\mathbf{q} = \mathbf{0}$, and its variation in the chemical energy ϕ_{chem} , see Eq. (5), leads to the increase/decrease of the transformation stress.

During the forward transformation ($\dot{\eta} > 0$), the adiabatic heat balance equation can be expressed as the following differential equation (here, with η playing the role of a pseudo-time)

$$\varrho_0 c \frac{dT}{d\eta} = \Delta s^* T + f_c, \quad T(0) = T_0, \quad (11)$$

and similarly during the reverse transformation ($\dot{\eta} < 0$) as

$$\varrho_0 c \frac{dT}{d\eta} = \Delta s^* T - f_c, \quad T(1) = T_m, \quad (12)$$

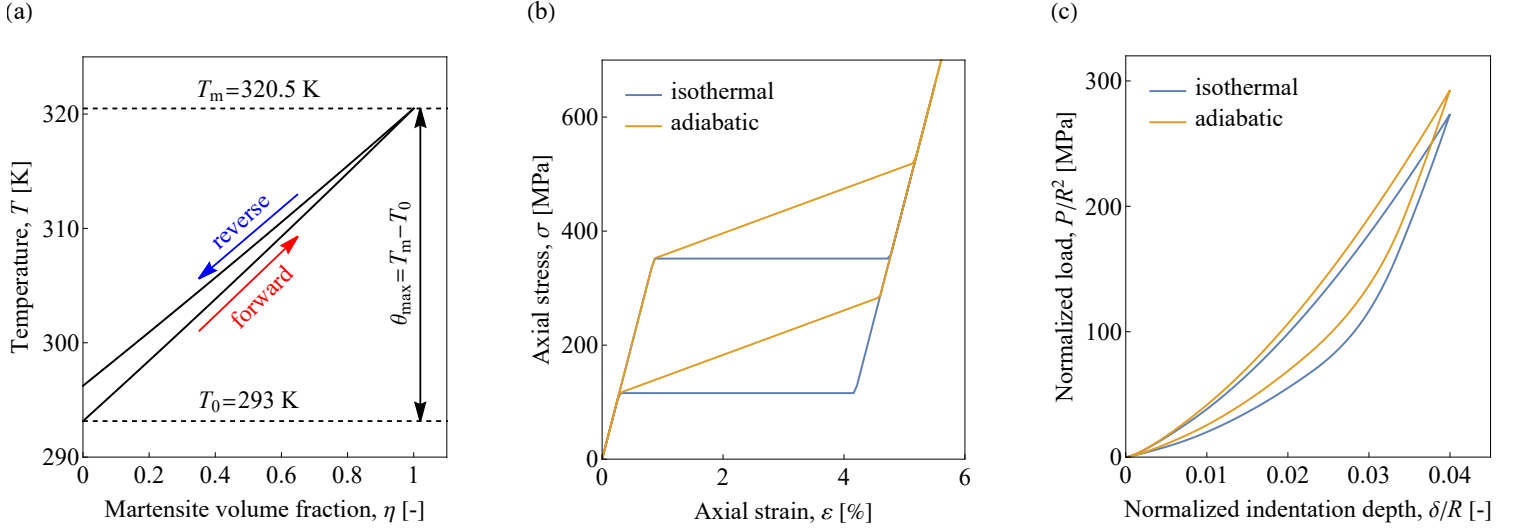


Figure 4: A simplified procedure to mimic a (fully) adiabatic condition in martensitic transformation: (a) temperature change during the forward and reverse transformation, (b) the material response for the isothermal and adiabatic cases, and (c) the load-indentation depth ($P/R^2 - \delta/R$) response for the isothermal and adiabatic cases. The calculations are performed for the initial temperature of $T_0 = 293$ K. The material parameters are the same as those introduced in Section 2.2.

where T_m denotes the initial temperature of reverse transformation. The differential equations (11) and (12) yield the following evolution equations for T as a function of the martensite volume fraction η , respectively,

$$T - T_0 = \left(T_0 + \frac{f_c}{\Delta s^*} \right) (e^{\eta \Delta s^* / \rho_0 c} - 1), \quad (13)$$

and

$$T - T_m = \left(T_m - \frac{f_c}{\Delta s^*} \right) (e^{(\eta-1) \Delta s^* / \rho_0 c} - 1). \quad (14)$$

Fig. 4(a) depicts the evolution of temperature T over a complete cycle of adiabatic forward and reverse transformation. In view of the contribution of the mechanical dissipation as a heat source, the temperature at the end of the cycle is marginally higher than the initial temperature T_0 . In Fig. 4(b), the adiabatic trilinear material response is compared with its isothermal counterpart. In the adiabatic case, the change in the chemical energy ϕ_{chem} induces a pronounced hardening behavior within the transformation regime. This, in turn, results in a load-indentation depth response with visibly higher loads compared to the isothermal case with a flat material response, as shown in Fig. 4(c). In fact, this adiabatic response represents an upper-bound of the potential thermal effects in the indentation problem.

3.2. Adiabatic Indentation vs. Isothermal Indentation

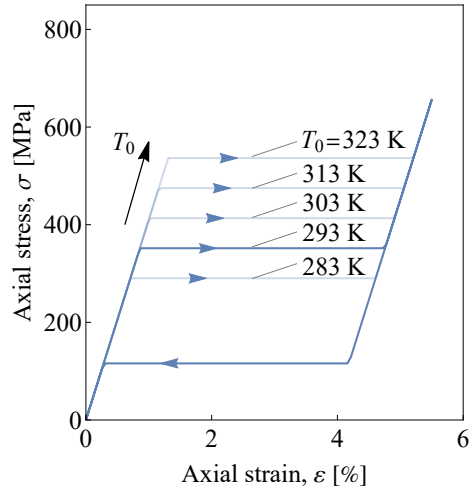
We carry out a comparative analysis to highlight the changes induced by the adiabatic condition with reference to the isothermal condition. Key quantities characterizing the indentation behavior

are assessed, namely the hysteresis loop area A_{hys} , the volume of the transformed region V_{tr} , and the indentation hardness H . We investigate how these characteristic quantities vary with initial temperature T_0 across different indentation depths δ . Specifically, we consider the temperature range of $283 \leq T_0 \leq 323$ K. The problem setup and the material parameters are the same as those in Section 2.2. Since the problem is now scale-independent, the findings remain the same regardless of the spatial scale of the analysis which is defined by the indenter radius R . Therefore, all results are presented in a normalized format. As previously, the indenter radius R is selected as the normalization parameter.

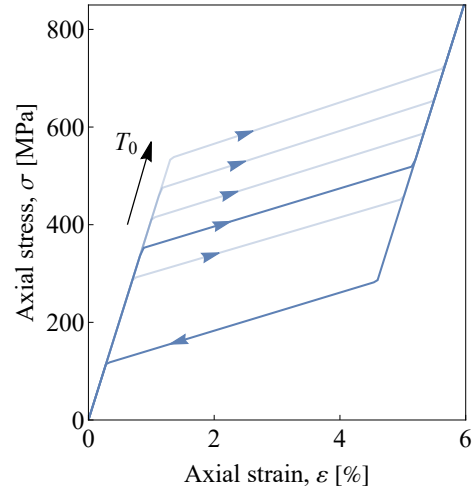
It is pertinent to begin the discussion by examining the effect of initial temperature T_0 on the material and load-indentation depth responses, as this facilitates the interpretation of the main analysis outcome presented subsequently. Fig. 5 illustrates this effect for the isothermal and adiabatic scenarios. It follows from Fig. 5(a,b) that as T_0 increases, the transformation stress during the forward transformation (and obviously during the reverse transformation) increases. As a consequence, as can be seen from Fig. 5(c,d), the indentation loads increase with higher T_0 . Additionally, Fig. 5(c,d) indicates that the hysteresis loop area A_{hys} exhibits a noticeable variation as a function of T_0 , a point that will be elaborated later on. Another important aspect to include in this discussion concerns the evolution of the (full-cycle) load-indentation depth response as a function of the maximum indentation depth δ_{max} , as illustrated in Fig. 6(a). A notable observation from Fig. 6(a) is that, irrespective of δ_{max} , the unloading branch consistently traces the same path. This suggests that the hysteresis loop area A_{hys} likely exhibits a straightforward relationship with δ_{max} . Finally, to complement the initial observations, Fig. 6(b,c) showcases the progression of the transformed region at different indentation depths δ . At each stage of transformation, the transformed region is divided into two distinct zones: a fully-transformed zone with martensite volume fraction of $\eta = 1$ and a partially-transformed zone with $0 < \eta < 1$. It is evident from Fig. 6(c) that as the indentation depth δ increases, not only the fully-transformed zone but also the partial one grows in size. The results presented in Fig. 6 correspond to the isothermal scenario, however, similar observations are applicable to the adiabatic scenario.

We now turn to the discussion of the characteristic quantities introduced earlier. Fig. 7 summarizes the overall behavior of the hysteresis loop area A_{hys} and the volume of the transformed region V_{tr} , the latter defined as the volume integral of the martensite volume fraction η . Both quantities are normalized by R^3 . Given the volumetric nature of V_{tr} , R^3 is a natural choice for normalization factor. Moreover, R^3 arises automatically as the normalization factor for the hysteresis loop area A_{hys} when A_{hys} is computed directly from the normalized load-indentation depth ($P/R^2 - \delta/R$) response. As shown in Fig. 7, an identical trend is visible for both A_{hys} and V_{tr} (this is because the hysteresis area A_{hys} , i.e., dissipation, is related to the transformed volume V_{tr} through the relation

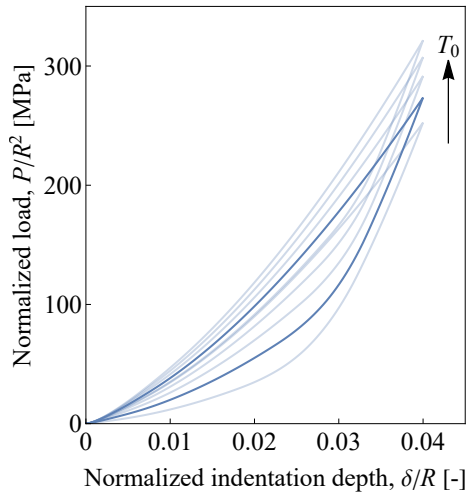
(a) material responses: isothermal



(b) material responses: adiabatic



(c) indentation responses: isothermal



(d) indentation responses: adiabatic

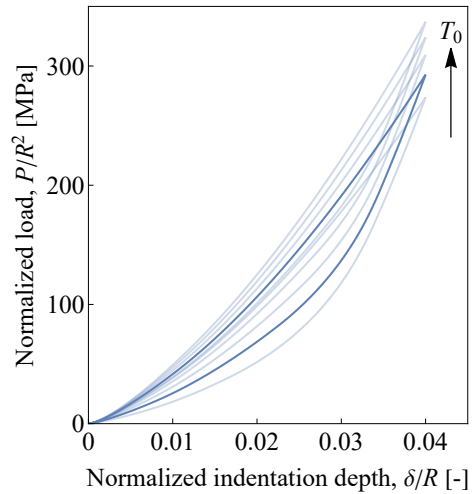


Figure 5: The effect of the initial temperature T_0 on the stress–strain (σ – ϵ) material response (a,b), and the load–indentation depth (P/R^2 – δ/R) response (c,d) in isothermal and adiabatic conditions. In panels (a,b), the full pseudoelastic loop is shown for $T_0 = 293$ K, while only the loading branches are shown for the other temperatures. Accordingly, in panels (c,d), only the indentation response for $T_0 = 293$ K is presented in full color.

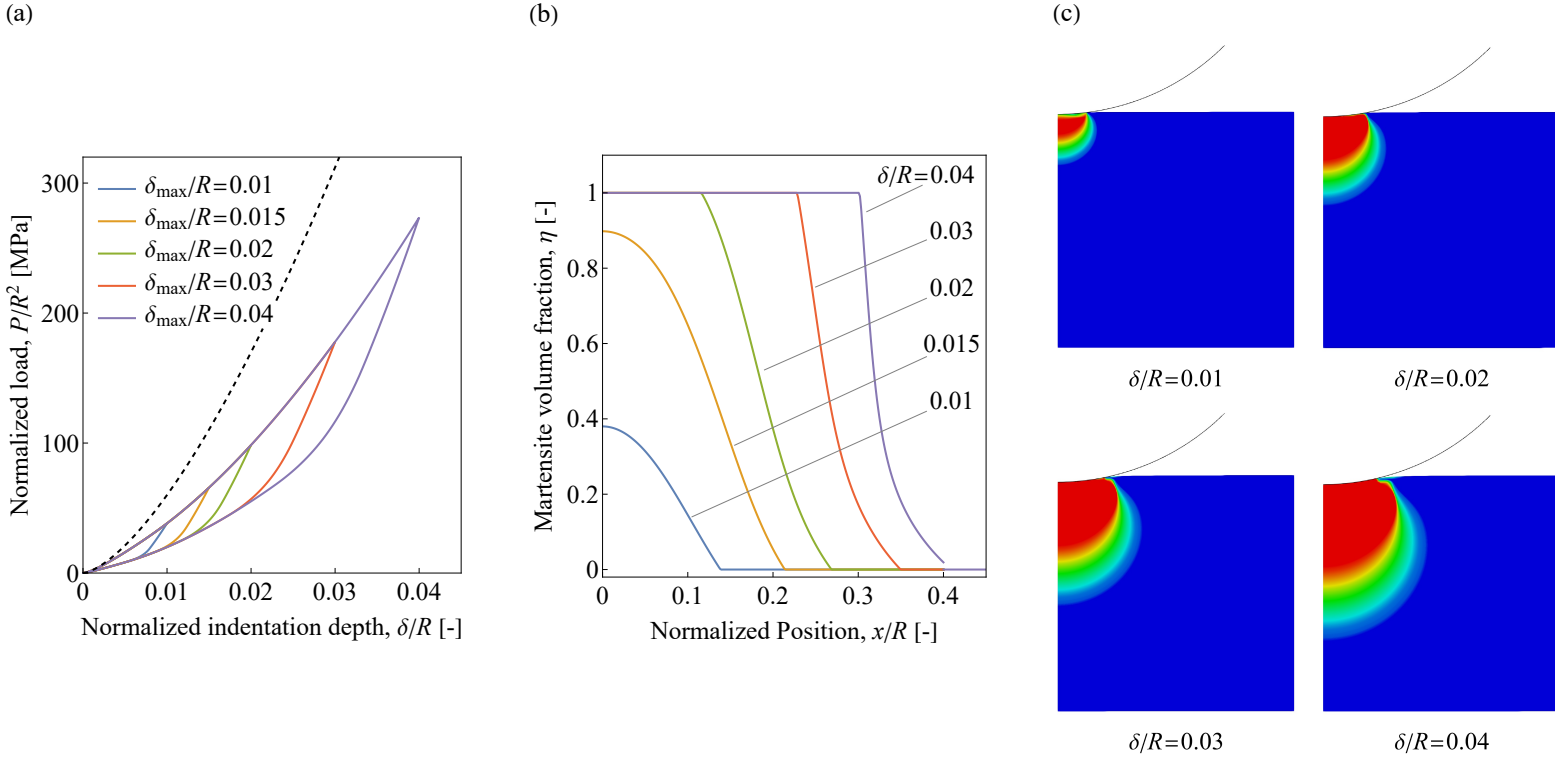


Figure 6: Simulation results for the isothermal indentation at an initial temperature of $T_0 = 293$ K: (a) full-cycle load-indentation depth ($P/R^2 - \delta/R$) response for various maximum indentation depths, and (b,c) profiles of the martensite volume fraction η and snapshots of the transformed domain at different indentation depths. The profiles in panel (b) are taken at a normalized vertical position of $y/R = 0.16$ beneath the indenter.

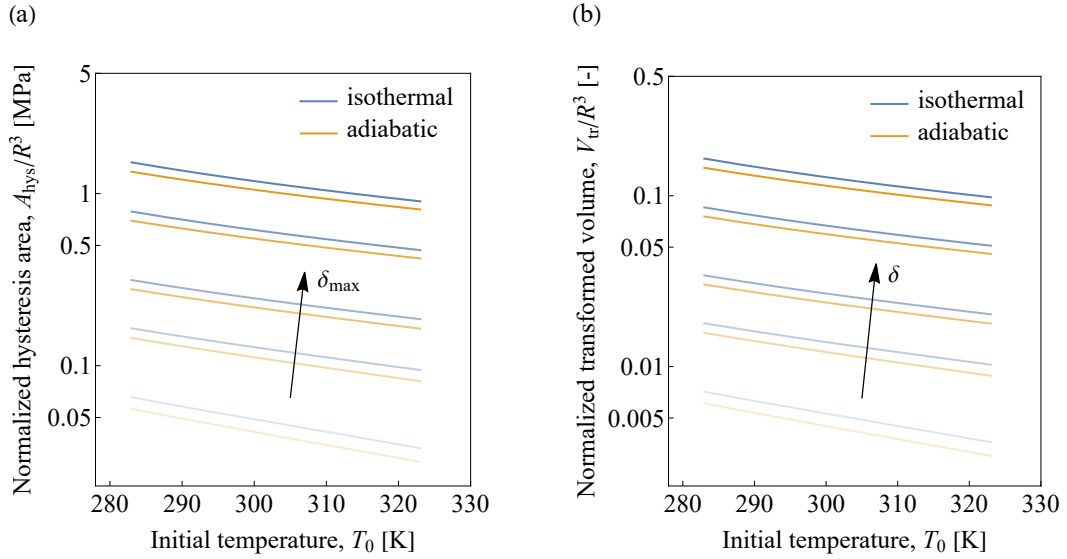


Figure 7: Hysteresis loop area A_{hys} (a) and volume of the transformed region V_{tr} (b) as a function of the initial temperature T_0 and the indentation depth. Note the logarithmic-linear scale in both plots.

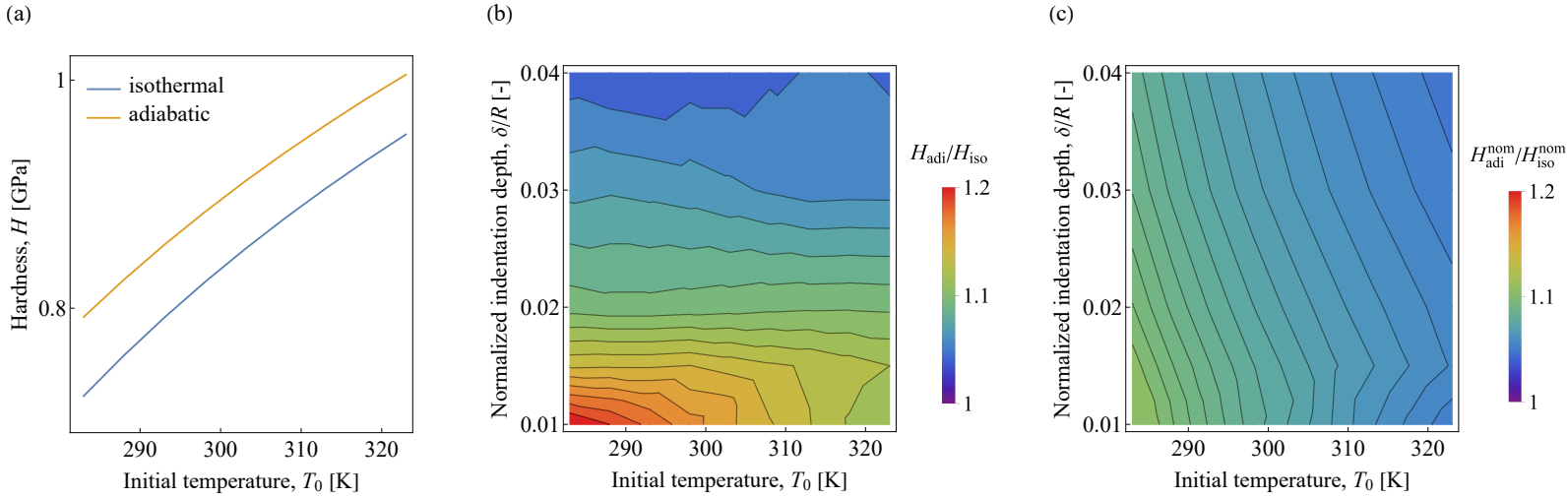


Figure 8: Indentation hardness H : (a) the individual adiabatic and isothermal curves for varying initial temperature T_0 at a normalized indentation depth of $\delta/R = 0.02$, (b) contour plot of the hardness ratio $H_{\text{adi}}/H_{\text{iso}}$ as a function of the initial temperature T_0 and the normalized indentation depth δ/R , and (c) contour plot of the nominal hardness ratio $H_{\text{adi}}^{\text{nom}}/H_{\text{iso}}^{\text{nom}}$, with the hardness values $H_{\text{adi}}^{\text{nom}}$ and $H_{\text{iso}}^{\text{nom}}$ calculated using the nominal contact area A_c^{nom} .

$A_{\text{hys}} = 2f_c V_{\text{tr}}$). More specifically, they both decline with increasing initial temperature T_0 . Also, the gap between the adiabatic and isothermal curves becomes more pronounced as the indentation depth δ (δ_{max} for A_{hys}) increases (note the logarithmic scale in the vertical axes). Finally, the isothermal curve always lies above the corresponding adiabatic one. The latter effect is obviously an outcome of the hardening-type behavior in the adiabatic scenario, which results in a reduced indentation-induced transformation compared to the isothermal scenario, and hence a reduction in both the hysteresis loop area A_{hys} and the transformed volume V_{tr} . By similar reasoning, the observed decreasing trend of the individual curves with increasing T_0 is also attributed to the increase of the transformation stress with T_0 (the Clausius–Clapeyron relation), as shown in Fig. 5(a,b), which, in turn, leads to a reduced transformation.

Finally, the results pertaining to the indentation hardness H are discussed. The hardness H is defined as

$$H = \frac{P}{A_c}, \quad (15)$$

where A_c , the contact area, is obtained from the finite-element solution and corresponds to the same instant as the load P . As commented in Section 2.2, the finite-element mesh within the contact region has been significantly refined, ensuring that A_c , and thus hardness H , are computed with a reasonable accuracy. Fig. 8(a) illustrates the relationship between the hardness H and the initial temperature T_0 at a normalized indentation depth of $\delta/R = 0.02$. Two immediate observations emerge from Fig. 8(a): the adiabatic condition results in a higher hardness, and hardness increases with rising T_0 . Both effects are connected with the increase in the transformation stress, governed

by the hardening-type behavior and the Clausius–Clapeyron relation, respectively.

It is insightful to evaluate carefully the correlation between the adiabatic and isothermal hardness values (denoted, respectively, as H_{adi} and H_{iso}). Fig. 8(b) provides a contour plot of the hardness ratio $H_{\text{adi}}/H_{\text{iso}}$ over the entire range of indentation depth δ and initial temperature T_0 analyzed. The plot reveals that $H_{\text{adi}}/H_{\text{iso}}$ reaches its maximum at the smallest values of δ and T_0 , while also exhibiting a higher rate of change within this region. Conversely, as δ and T_0 increase, $H_{\text{adi}}/H_{\text{iso}}$ approaches unity, and at the same time, its rate of change diminishes. Concerning the influence of T_0 , we note that the ratio between the total energy supplied to the system and the dissipated energy increases with increasing T_0 (as evident from the comparison between the area beneath the loading branch of the material response and the corresponding hysteresis loop area in Fig. 5(a,b)). As a result, the type of the response within the transformation regime, hardening-type or flat, makes relatively smaller contribution to the indentation response for higher T_0 , and this leads to a closer alignment between the adiabatic and isothermal loads. Concerning the influence of δ , we note that a larger volume of material undergoes complete transformation at higher δ and the corresponding material response enters the stiff elastic branch of martensite, within which the adiabatic and isothermal cases behave the same.

It is important to remark here on the challenge of determining the contact area in experiments. In standard elasto-plastic materials, where unloading primarily involves elastic recovery, the contact area is either measured directly from the residual imprint or estimated analytically following the Oliver and Pharr method [19]. In pseudoelastic SMAs, however, the reverse phase transformation that takes place during unloading causes the martensitic microstructure to recover (fully or partially), resulting in a residual imprint (if any) that does not represent genuinely the actual contact area under the maximum load [20], see also [21] for a more detailed discussion. A common approach to circumvent this issue is to use the nominal contact area, defined by simple geometrical considerations in terms of the indenter radius R and the indentation depth δ , as $A_c^{\text{nom}} = \pi\delta(2R - \delta)$. In fact, the nominal contact area is also adopted for elasto-plastic materials, as a means to sidestep the experimental error resulting from the direct measurement of the contact area from the residual imprint [22].

Fig. 8(c) presents the contour plot of the nominal hardness ratio $H_{\text{adi}}^{\text{nom}}/H_{\text{iso}}^{\text{nom}}$, with hardness values being evaluated using the nominal contact area A_c^{nom} . Evidently, when A_c^{nom} is employed, a milder discrepancy is obtained between the adiabatic and isothermal hardness values. A comparison of the contour plots in Fig. 8(b,c) reveals that the variation in the actual contact area A_c does not follow the same trend as the indentation load P (notice that the the nominal hardness ratio $H_{\text{adi}}^{\text{nom}}/H_{\text{iso}}^{\text{nom}}$ actually represents the ratio between the corresponding indentation loads). At lower indentation depths, A_c in the adiabatic case is smaller than its isothermal counterpart, thus A_c acts

in concert with P to yield a larger ratio $H_{\text{adi}}/H_{\text{iso}}$. At higher indentation depths, however, A_c in the adiabatic case becomes larger than its isothermal counterpart, thus A_c counteracts with P to diminish the discrepancy between H_{iso} and H_{adi} .

4. Summary and Discussion

In SMAs, thermomechanical coupling interactions manifest in two primary aspects: the effect of ambient temperature, governed by the Clausius–Clapeyron relation, and the transient effect of latent heat of martensitic transformation. Both aspects are examined in the present study. Our analysis in Section 2.2 demonstrates that thermomechanical coupling arising from the latent heat of transformation is of limited significance within the spatial and temporal scales relevant to quasi-static micro/nano-indentation problems. The results indicate that due to the predominant role of heat conduction, temperature gradients remain negligible, resulting in only a marginal influence on the indentation response. On the other hand, the analysis in Section 3.2, while underscoring the significant role of initial (ambient) temperature, reveals that even in the (hypothetical) adiabatic scenario, the simulation results do not show a substantial qualitative deviation from those in the isothermal scenario, thereby further highlighting the minor role of latent heat of transformation during indentation. This conclusion is supported by the observation that the volume of the transformed region V_{tr} , and likewise the hysteresis loop area A_{hys} , exhibit trends qualitatively similar in adiabatic and isothermal conditions, and also the related quantitative differences are not too high. Moreover, concerning the indentation hardness, the most significant variations occur at shallow indentations (and at low initial temperatures), a range that, given the limited volume of phase transformation, may not be the primary focus of interest in actual applications. By and large, our study suggests that incorporating thermal effects arising from the latent heat is not of critical importance when analyzing indentation-induced martensitic transformation, especially at small spatial scales.

Since the main focus of the present study is on thermal effects, we have significantly simplified the SMA constitutive description. We assume an isotropic material with no tension–compression asymmetry and adopt a flat trilinear intrinsic material response. However, in reality, polycrystalline (textured) NiTi typically displays a strong transverse isotropy with a visible tension–compression asymmetry. Also, the material possesses a softening-type material response in tension and a hardening-type response in compression [23, 24]. Nevertheless, we anticipate that our findings on thermomechanical interactions remain qualitatively the same regardless of the underlying constitutive relations adopted. It is also important to note that the softening-type behavior in NiTi tends to promote strain localization in thin specimens under tensile loads. However, since indentation is primarily associated with compressive stresses and involves bulk materials, the localization

effects are expected to have limited relevance.

Our supplementary analysis on cyclic indentation (with an indenter radius of $R = 0.5$ mm and an indentation speed of $v = 1$ $\mu\text{m/s}$, not reported in detail here) reveals that after the loading stage of the 10th indentation cycle, the maximum temperature rise beneath the indenter is about $\theta_{\max} = 0.017$ K (i.e., about 1.5 times higher than $\theta_{\max} = 0.011$ K recorded after the loading stage of the first cycle, cf. Fig. 3), which is too small to induce any noticeable effect. This shows that even under repeated loading, the thermal effects remain negligible, reinforcing the conclusion that transient thermomechanical coupling effects are unlikely to play a major role in small-scale indentation.

We emphasize again that the central focus of the current study has been to demonstrate the role of thermomechanical coupling effects in the indentation behavior of pseudoelastic SMAs. Our investigation is thus hinged on the assumption that pseudoelasticity is the unique inelastic mechanism at play. This assumption is justifiable given the use of spherical indenter and not targeting large indentation depths. Indeed, a handful of experimental studies have reported a complete recovery of inelastic deformation under shallow spherical indents, see e.g., [8, 25, 26]. It is, however, important to note that in micro/nano-indentation experiments, dislocation plasticity has been commonly identified as an undeniable contributor to the inelastic deformation. Therefore, incorporating plasticity (both austenite yielding and transformation-induced plasticity) would provide a more comprehensive insight into the indentation behavior and the related rate effects, and this constitutes a valuable direction for future research.

Acknowledgements. This work has been supported by the National Science Centre (NCN) in Poland through the Grant No. 2021/43/D/ST8/02555. For the purpose of Open Access, the authors have applied a CC-BY public copyright license to any Author Accepted Manuscript (AAM) version arising from this submission.

Data availability

Data will be made available on request.

References

- [1] J. A. Shaw, S. Kyriakides, Thermomechanical aspects of NiTi, *J. Mech. Phys. Solids* 43 (1995) 1243–1281.
- [2] X. Zhang, P. Feng, Y. He, T. Yu, Q. P. Sun, Experimental study on rate dependence of macroscopic domain and stress hysteresis in NiTi shape memory alloy strips, *Int. J. Mech. Sci.* 52 (2010) 1660–1670.

- [3] Y. Xiao, D. Jiang, Rate dependence of transformation pattern in superelastic NiTi tube, *Extreme Mech. Lett.* 39 (2020) 100819.
- [4] S. Tsimpoukis, S. Kyriakides, Rate induced thermomechanical interactions in niti tensile tests on strips, *J. Mech. Phys. Solids* 184 (2024) 105530.
- [5] K. Gall, K. Juntunen, H. J. Maier, H. Sehitoglu, Y. I. Chumlyakov, Instrumented micro-indentation of NiTi shape-memory alloys, *Acta Mater.* 49 (2001) 3205–3217.
- [6] C. P. Frick, T. W. Lang, K. Spark, K. Gall, Stress-induced martensitic transformations and shape memory at nanometer scales, *Acta Mater.* 54 (2006) 2223–2234.
- [7] J. Pfetting-Micklich, C. Somsen, A. Dlouhy, C. Begau, A. Hartmaier, M. F.-X. Wagner, G. Eggeler, On the crystallographic anisotropy of nanoindentation in pseudoelastic NiTi, *Acta Mater.* 61 (2013) 602–616.
- [8] S. Kumar S, I. A. Kumar, L. Marandi, I. Sen, Assessment of small-scale deformation characteristics and stress-strain behavior of NiTi based shape memory alloy using nanoindentation, *Acta Mater.* 201 (2020) 303–315.
- [9] A. Amini, Y. He, Q. Sun, Loading rate dependency of maximum nanoindentation depth in nano-grained NiTi shape memory alloy, *Mat. Lett.* 65 (3) (2011) 464–466.
- [10] A. Amini, C. Cheng, Q. Kan, M. Naebe, H. Song, Phase transformation evolution in NiTi shape memory alloy under cyclic nanoindentation loadings at dissimilar rates, *Sci. Rep.* 3 (2013) 3412.
- [11] H. Li, Z. Gao, J.-Y. Suh, H. N. Han, U. Ramamurty, J.-i. Jang, On the superelastic behavior during spherical nanoindentation of a Ni-Ti shape memory alloy, *Materialia* 33 (2024) 102020.
- [12] M. Rezaee-Hajidehi, K. Tuma, S. Stupkiewicz, Gradient-enhanced thermomechanical 3D model for simulation of transformation patterns in pseudoelastic shape memory alloys, *Int. J. Plast.* 128 (2020) 102589.
- [13] M. Rezaee Hajidehi, S. Stupkiewicz, Gradient-enhanced model and its micromorphic regularization for simulation of Lüders-like bands in shape memory alloys, *Int. J. Solids Struct.* 135 (2018) 208–218.
- [14] A. Sadjadpour, K. Bhattacharya, A micromechanics-inspired constitutive model for shape-memory alloys, *Smart Mater. Struct.* 16 (2007) 1751.
- [15] K. Otsuka, X. Ren, Physical metallurgy of Ti–Ni-based shape memory alloys, *Prog. Mat. Sci.* 50 (2005) 511–678.

- [16] J. Korelc, P. Wriggers, *Automation of Finite Element Methods*, Springer International Publishing, Switzerland, 2016.
- [17] P. Alart, A. Curnier, A mixed formulation for frictional contact problems prone to newton like solution methods, *Comp. Meth. Appl. Mech. Engng.* 92 (1991) 353–375.
- [18] S. Stupkiewicz, *Micromechanics of contact and interphase layers*, Springer Berlin Heidelberg, 2007.
- [19] W. C. Oliver, G. M. Pharr, An improved technique for determining hardness and elastic modulus using load and displacement sensing indentation experiments, *J. Mat. Res.* 7 (1992) 1564–1583.
- [20] R. Liu, D. Y. Li, Y. S. Xie, R. Llewellyn, H. M. Hawthorne, Indentation behavior of pseudoe-
lastic TiNi alloy, *Scripta Mat.* 41 (1999) 691–696.
- [21] M. Rezaee-Hajidehi, K. Tüma, S. Stupkiewicz, Indentation-induced martensitic transformation
in smas: Insights from phase-field simulations, *Int. J. Mech. Sci.* 245 (2023) 108100.
- [22] H. Petryk, S. Stupkiewicz, S. Kucharski, On direct estimation of hardening exponent in crystal
plasticity from the spherical indentation test, *Int. J. Solids Struct.* 112 (2017) 209–221.
- [23] J. F. Hallai, S. Kyriakides, Underlying material response for Lüders-like instabilities, *Int. J.*
Plast. 47 (2013) 1–12.
- [24] B. Reedlunn, C. B. Churchill, E. E. Nelson, J. A. Shaw, S. H. Daly, Tension, compression, and
bending of superelastic shape memory alloy tubes, *J. Mech. Phys. Solids* 63 (2014) 506–537.
- [25] W. Yan, Q. Sun, H.-Y. Liu, Spherical indentation hardness of shape memory alloys, *Mat. Sci.*
Engng. A 425 (2006) 278–285.
- [26] M. Arciniegas, Y. Gaillard, J. Pena, J. M. Manero, F. J. Gil, Thermoelastic phase transforma-
tion in TiNi alloys under cyclic instrumented indentation, *Intermetallics* 17 (2009) 784–791.